

See discussions, stats, and author profiles for this publication at: <https://www.researchgate.net/publication/314163212>

Shear Strength Enhancement Mechanisms of Steel Fiber-Reinforced Concrete Slender Beams

Article in ACI Structural Journal · May 2017

DOI: 10.14359/51689449

CITATIONS

66

READS

2,701

2 authors, including:



Shih-Ho Chao

The University of Texas at Arlington

113 PUBLICATIONS 3,230 CITATIONS

[SEE PROFILE](#)

Title No. 114-S59

Shear Strength Enhancement Mechanisms of Steel Fiber-Reinforced Concrete Slender Beams

by Mohammad Reza Zarrinpour and Shih-Ho Chao

An experimental study was conducted to identify the shear-enhancement and failure mechanisms behind the ultimate shear strength of steel fiber-reinforced concrete (SFRC) slender beams by using the full-field-deformation-measuring capability of digital image correlation (DIC) technology. A total of 12 large-scale simply supported SFRC and RC beams with an overall height from 12 to 48 in. (305 to 1220 mm) were tested under monotonic point load up to failure. The greater shear strength in SFRC beams originates from the ability of the fiber bridging effect that delays the propagation of the cracks into the compression zone, whose shear strength is enhanced by the compressive stresses induced by the higher load. The slow progression of the cracks keeps the compression zone depth large, thereby enabling it to contribute to a higher shear resistance. In contrast with the traditional assumption for either plain concrete or SFRC beams, where the shear contribution resulting from dowel action is completely neglected, this research clearly shows that the dowel action has an appreciable effect on the ultimate shear strength. Its contribution varies from 10 to 30% when the beam depth increases from 12 to 48 in. (305 to 1220 mm). On the other hand, the compression zone's contribution decreases from 69 to 36% with the increase in beam depth. In addition, the shear contribution from the fiber bridging effect along the critical shear crack stays approximately unchanged at 20%, irrespective of the beam depth. In this study, the minimum shear strength obtained was in the range of $5\sqrt{f'_c}$ psi (0.42 $\sqrt{f'_c}$ MPa) for the beams with the greatest depth. This indicates that the maximum allowed shear stress limit of $1.5\sqrt{f'_c}$ psi (0.125 $\sqrt{f'_c}$ MPa) specified in ACI 318-14 is on the very conservative side.

Keywords: dowel action; hooked-end steel fiber; shear strength; steel fiber-reinforced concrete.

INTRODUCTION

While there is a rather universal acknowledgement of diagonal shear failure in plain concrete (PC) beams (without transverse reinforcement), different models with distinct perspectives have been proposed to explain the shear resistance mechanism of PC beams. One explanation is found in the Modified Compression Field Theory (Vecchio and Collins 1986), where the aggregate interlock (based on aggregate sizes), crack width/spacing, and straining effect due to longitudinal reinforcement are used to explain the shear behavior. Another popular approach is the Compression Force Path Theory (Kotsovos 1988) in which the resistance against shear is assumed to be provided by a compression path through which the external force is transmitted to the supports. Finally, the Critical Shear Crack Theory (Muttoni and Fernández Ruiz 2008) introduces arch action as the possible shear-carrying mechanism of a PC beam upon formation of a critical shear crack.

Generally, the mechanical behavior of fiber-reinforced concrete (FRC) is significantly different from PC, depending on the fiber volume fraction, fiber geometry, fiber orientations, and fiber-to-matrix bond characteristics. Numerous studies have shown that steel fiber-reinforced concrete (SFRC) can considerably improve the post-cracking tensile behavior and toughness of concrete (Mobasher 2012). When considering SFRC behavior at the structural element scale, the addition of steel fibers in concrete beams can also result in a substantial increase in the ultimate shear capacity in comparison with identical plain concrete beams. The enhanced shear strength is usually attributed to the fiber bridging stress across shear cracks (Choi et al. 2007). For design purposes, ACI Committee 318 (2014) allows the use of steel fibers as minimum shear reinforcement when $\phi 0.5v_c \leq v_u \leq \phi v_c$, where compressive strength of concrete does not exceed 6 ksi (41 MPa), depth is no more than 24 in. (610 mm), and shear stress v_u is no more than $\phi 2\sqrt{f'_c}$ (that is, $1.5\sqrt{f'_c}$ where f'_c is in psi). ACI Committee 318 (2014) also requires a minimum volume fraction of steel fibers of 0.75% (100 lb steel fibers per cubic yard of concrete). To date, a limited number of models have been proposed for the shear resistance mechanisms of SFRC beams. Choi et al. (2007) proposed a theoretical strain-based model to account for the effect of flexural deformation on shear capacity of an SFRC beam. The shear resistance from aggregate interlock and dowel action has been ignored because the intact compression zone was assumed to prevent slip of the crack interface (Choi et al. 2007; Kotsovos and Pavlović 1998). They assumed that the shear resistance of an SFRC beam is provided by the intact compression zone and the bridging tensile strength of steel fibers crossing the critical shear crack. The location of the critical shear crack was first determined by their strain-based formulations through an iterative process, and then the shear contribution of the compression zone was determined by Rankin's failure criteria. Contrary to the procedure used by Choi et al. (2007), in this study, the full field strains (thus, stresses) were measured by digital image correlation (DIC) directly along the critical crack right before failure, thereby eliminating any assumption and iterative procedure to establish shear strength. Dinh et al. (2011) used a similar approach where the shear contribution of

ACI Structural Journal, V. 114, No. 3, May-June 2017.

MS No. S-2016-005.R2, doi: 10.14359/51689449, received July 7, 2016, and reviewed under Institute publication policies. Copyright © 2017, American Concrete Institute. All rights reserved, including the making of copies unless permission is obtained from the copyright proprietors. Pertinent discussion including author's closure, if any, will be published ten months from this journal's date if the discussion is received within four months of the paper's print publication.

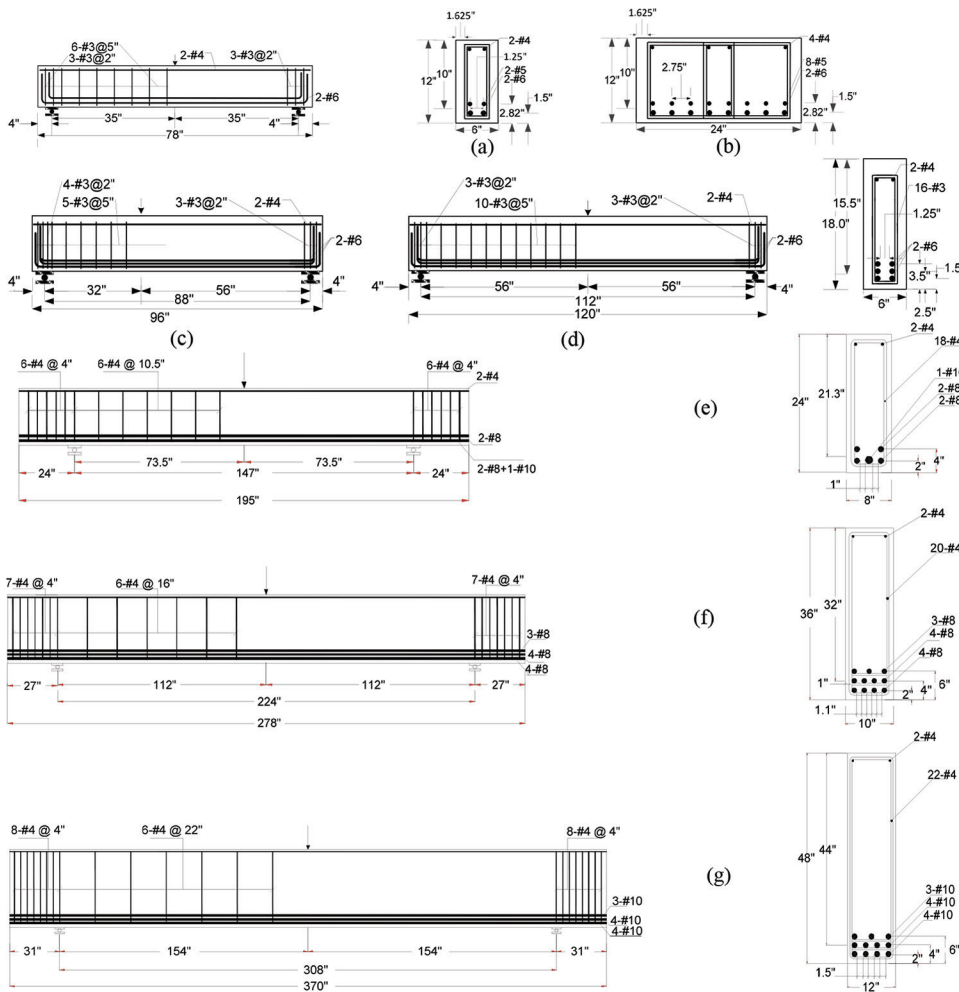


Fig. 1—Geometry and reinforcement details of large-scale RC and SFRC beams: (a) SFRC12W6; (b) SFRC12W24; (c) RC18; (d) SFRC18; (e) SFRC24; (f) SFRC36; and (g) SFRC48. (Note: 1 in. = 25.4 mm.)

aggregate interlock and dowel action were ignored. Dinh et al. (2010) reported that 18 of the 23 SFRC specimens failing in shear were caused by tension failure. Nevertheless, in their model, they assumed that crushing in the compression zone was the cause of failure, and employed the compression failure criterion established for plain concrete by Bresler and Pister (1958) with the average ultimate compressive stress of $0.85f'_c$ in Whitney's stress block.

In general, the current models used to predict the ultimate shear strength of SFRC beams were developed on the basis of simplified assumptions concerning shear failure mechanism. Even though some shear-resisting components have proven negligible for RC beams, their contribution to SFRC beams has not yet been assessed. Furthermore, the strength-enhancement mechanism of SFRC beams is still not well defined. Establishment of the strength-enhancement mechanism serves as a preliminary step to investigate size effect in ultimate shear strength of SFRC beams and to determine the design shear strengths of SFRC beams, which has a conservative low value in current ACI 318 provisions (ACI Committee 318 2014). This research aims at determining the shear-enhancement and failure mechanisms of SFRC beams by means of a deformation-monitoring digital image correlation (DIC) technique. DIC captures full field deformations and their progression with load increase.

RESEARCH SIGNIFICANCE

Shear strength-enhancement and the resistance mechanism of SFRC beams were assessed. The primary components were identified through experiments on large-scale SFRC beams with a range of depths varying from 12 to 48 in. (305 to 1220 mm). The results obtained from this experimental study were particularly valuable because of the full field deformation (that is, state of strain on each arbitrary plane and displacement in all directions) obtained from DIC. Identification of the key factors contributing to the shear strength was performed based on the visualization of strains and deformations provided by the DIC as well as a mechanical-based computation.

EXPERIMENTAL PROGRAM

Specimens

A total of 12 simply supported SFRC and RC beams were monotonically loaded up to failure. Each pair out of the first four pairs of SFRC beams consisted of two duplicated beams, whereas the last pair had two identical SFRC specimens differing in width (6 and 24 in. [152 and 610 mm]), which allowed the investigation of the effect of width on the shear behavior of SFRC beams (Fig. 1(a) and 1(b)). Two identical RC beams with no stirrup and an overall height of 18 in. (457 mm) were used as control specimens. For all specimens,

Table 1—Design properties of specimens

Specimen	Width b , in. (mm)	Height h , in. (mm)	Effective depth d , in. (mm)	a/d	ρ , %	V_f , %	Targeted f'_c , psi (MPa)	Measured f'_c , psi (MPa)
SFRC12W6	6 (152)	12 (305)	10 (254)	3.5	2.5	0.75	6000 (42)	4235 (29)
SFRC12W24	24 (610)	12 (305)	10 (254)	3.5	2.5	0.75	6000 (42)	4235 (29)
SFRC18a,b	6 (152)	18 (457)	15.5 (394)	3.6	2.82	0.75	6000 (42)	5707 (39)
SFRC24a,b	8 (203)	24 (610)	21.3 (541)	3.45	2.64	0.75	6000 (42)	7210 (50)
SFRC36a,b	10 (254)	36 (915)	32 (813)	3.5	2.72	0.75	6000 (42)	7210 (50)
SFRC48a,b	12 (305)	48 (1220)	44 (1118)	3.5	2.65	0.75	6000 (42)	7210 (50)
RC18a,b	6 (152)	18 (457)	15.5 (394)	3.6	2.82	0	6000 (42)	5514 (38)

Table 2—Mixture proportions by weight

Type of mixture	Cement (Type I)	Fly ash (Class C)	Sand	Coarse aggregate 3/8 in. (10 mm)	Water*	Steel fiber	Total weight
SFRC	1.00	0.5	1.7	1.00	0.45	0.117†	4.77
RC	1.00	0.5	1.7	1.00	0.45	0	4.65

*w/cm = 0.3.

† $V_f = 0.75\%$.

the following parameters were held constant: shear span to effective depth ratio (a/d); longitudinal reinforcement ratio (ρ); steel fiber volume fraction (V_f); fiber type; and design concrete compressive strength. For the SFRC specimens, effective depth was selected as the only parameter varying from one pair to another, which in turn led the beams to have overall heights of 12, 18, 24, 36, and 48 in. (305, 457, 610, 915, and 1220 mm). Fibers were hooked-end steel fibers ($l/d = 67$, $l = 2.0$ in. [51 mm], $d = 0.03$ in. [0.76 mm], $f_t = 159$ ksi [1096 MPa]) conforming to ASTM A820. The fiber content was fixed at 0.75% by volume (or 100 lb steel fibers per cubic yard of concrete), which is the minimum amount as specified by ACI Committee 318 (2014). The design compressive strength of concrete was 6000 psi (42 MPa) in compliance with the maximum allowable compressive strength for SFRC (ACI Committee 318 2014).

Prior research has shown that shear strength (in terms of stress) of RC beams is not a function of beam width (Kani et al. 1979; Lubell et al. 2004). Despite the fact that this finding had not been explored in the case of SFRC beams, it constituted a premise and was initially considered in the design of test specimens. However, the validity of this premise will be verified in this paper's following sections. The width of each specimen pair was determined by three required tasks: 1) to ensure that the required longitudinal steel bars had a proper cover thickness; 2) to ensure that the shear capacity of specimens (loading) did not exceed the capacity of the equipment and setup; 3) to minimize weight for ease of transportation and disposal.

It is well known that for PC beams the shear strength varies with shear span-depth ratio (ASCE-ACI Committee 426 1973; Wight and MacGregor 2012). The direct strut between loading and support has a great influence on shear strength when span-to-effective-depth ratio (a/d) is approximately less than 2.5. In this study, a/d was selected to be 3.5 to minimize the effect from direct strut. Sufficient flexural reinforcement ($\rho_{ave} = 2.66\%$) was provided to ensure that the failure was governed by shear rather than flexure.

The amount of the longitudinal reinforcement was calculated according to the highest shear capacity ($6\sqrt{f'_c}$ psi [$0.5\sqrt{f'_c}$ MPa]) reported by Parra-Montesinos (2006) for SFRC beams with $V_f = 0.75\%$. Note that research done by Shoaib et al. (2014) showed that longitudinal reinforcement ratio in the range of 1.44% to 4.03% has almost no effect on the ultimate shear strength of SFRC beams. A similar conclusion was also drawn by Dinh et al. (2010) using a longitudinal reinforcement ratio between 1.6% and 2.7%. Self-weight of specimens was also taken into consideration. Geometry and reinforcement details of the RC and SFRC beams are shown in Fig. 1. To ensure that shear failure would occur in the instrumented span, the other span was reinforced by stirrups as shown in Fig. 1. Mechanical terminators (headed bars) were employed at the end of the longitudinal bars to alleviate the congestion except for the 18 in. (457 mm) deep RC, and 12 and 18 in. (305 and 457 mm) SFRC beams in which the longitudinal bars were bent 90 degrees at the ends to provide anchorage. The design properties of specimens are listed in Table 1.

Mixture compositions and material properties

Table 2 gives the SFRC mixture proportions with a target maximum compressive strength of 6000 psi (42 MPa).

Test setup and instrumentation

SFRC specimens were loaded by a concentrated force at midspan through a 650 kip (2891 kN) hydraulic cylinder. For the RC beams, however, the load was applied at one-third of the span length (Fig. 1(c)). In each test, the beam was initially loaded until the first visible flexural crack surfaced. Then, loads were monotonically increased and paused at a few loadings to trace the cracks and take photos. The process continued until failure. For safety purposes, lateral supports were provided for specimens with depths of 36 and 48 in. (915 and 1220 mm). The lateral supports were not in contact with the specimen surface.

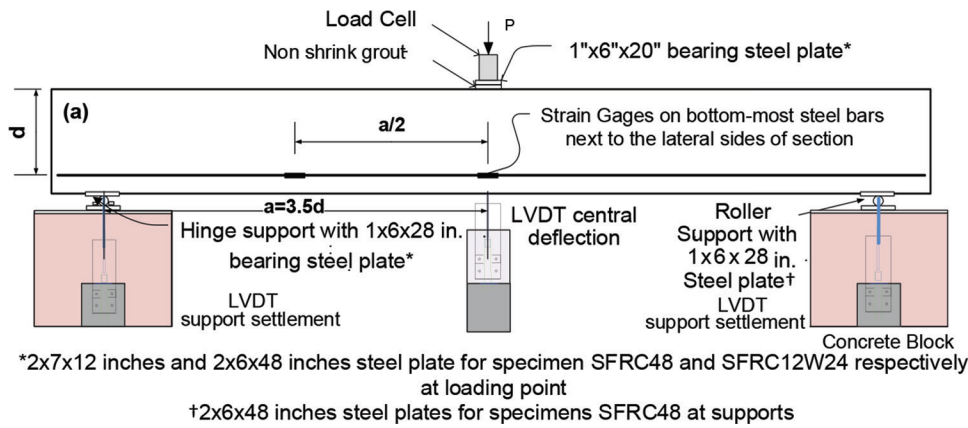


Fig. 2—Schematic view of test setup, loading configuration, and instrumentations. (Note: 1 in. = 25.4 mm.)

Table 3—Test results

Specimen	P_u , kip (kN)	V_u , kip (kN)	v_{u0} , psi (MPa)	$v_u/\sqrt{f'_c}$, $\sqrt{\text{psi}}$ ($\sqrt{\text{MPa}}$)	v_{cr} , psi (MPa)	C_w^* , in. (mm)	$Def^†$, in. (mm)
SFRC12W6	54 (240)	27 (120)	449.4 (3.1)	6.9 (0.57)	350.0 (2.41)	0.052 (1.32)	0.31 (7.9)
SFRC12W24	215 (956)	108 (478)	448.1 (3.1)	6.9 (0.57)	304.0 (2.09)	0.129 (3.28)	0.41 (10.4)
SFRC18a	73 (323)	36 (161)	389.7 (2.7)	5.2 (0.43)	241.9 (1.7)	0.054 (1.37)	0.58 (14.7)
SFRC18b	88 (389)	44 (194)	470.2 (3.2)	6.2 (0.52)	166.7 (1.1)	0.066 (1.66)	0.51 (13.0)
SFRC24a	120 (534)	60 (267)	352.3 (2.4)	4.2 (0.34)	234.7 (1.6)	0.060 (1.52)	0.42 (10.7)
SFRC24b	171(759)	85 (380)	500.9 (3.5)	5.9 (0.49)	176.1 (1.2)	0.080 (2.03)	0.65 (16.5)
SFRC36a	307 (1365)	154 (683)	479.6 (3.3)	5.7 (0.47)	125.0 (0.9)	0.080 (2.03)	0.92 (23.4)
SFRC36b	317 (1408)	158 (704)	494.5 (3.4)	5.8 (0.48)	187.5 (1.3)	0.041 (1.04)	0.78 (19.8)
SFRC48a	470 (2091)	235 (1045)	445.1 (3.1)	5.2 (0.44)	151.5 (1.0)	0.077 (1.96)	1.31 (33.3)
SFRC48b	454 (2017)	227 (1008)	429.4 (3.0)	5.1 (0.42)	132.6 (0.9)	0.101 (2.56)	1.26 (32.0)
RC18a	51 (226)	19 (82)	198.5 (1.4)	2.7 (0.22)	139.8 (1.0)	0.001 (0.04)	0.17 (4.3)
RC18b	45 (202)	17 (73)	177.3 (1.2)	2.4 (0.20)	118.3 (0.8)	0.014 (0.35)	0.15 (3.81)

*Maximum crack width at peak load.

†Beam deflection under loading point at ultimate load.

For each test, a total of three bearing plates were used at the supports and loading point. Dimensions of the bearing plate are illustrated in Fig. 2. To provide a uniform interface contact, a layer of non-shrink grout was used between the concrete and bearing plate at the loading point. With regard to the 24 in. (610 mm) wide specimen (SFRC12W24), to have the point load uniformly distributed over the width of the specimen, the load from hydraulic cylinder was transferred through a stiffened W12 x 87 steel beam to a 2 x 6 x 48 in. (51 x 152 x 1219 mm) bearing plate. A schematic view of the test setup, instrumentations, and loading configuration is depicted in Fig. 2. For each specimen, two pairs of strain gauges were mounted on the bottom-layer reinforcing bars at the location shown in Fig. 2. Three linear variable differential transformers (LVDTs) were employed to measure the deflections under the loading point and the settlement of each support. During the tests, the applied load was measured by a load cell. A DIC non-contact deformation measurement system with a measuring strain accuracy of 0.01% (in./in.) was used to view the full field of strains and displacements as they developed on the surface. One side of each specimen across the targeted shear span facing toward the cameras was regarded as a region of interest (ROI) and spackled by

stamping black paint dots on a white base. It was essential that each black dot contained at least 3 to 5 pixels for the DIC software to process the strain data with sufficient accuracy. Therefore, larger-size specimens with the same camera (five-megapixel camera) would require larger black dots to contain the required number of larger pixels. Testing was carried out 502 to 1005 days after casting. The specimens were exposed to weather during this period.

EXPERIMENTAL RESULTS AND DISCUSSION

The ultimate load P_u , average shear stress at failure v_u , shear strength normalized by $\sqrt{f'_c}$, and the maximum critical crack width at peak load C_w for all specimens are listed in Table 3. The strength-enhancement and resistance mechanisms of SFRC slender beams discussed in the following were deduced based on the observation of cracking patterns and visualization of the DIC-measured full field deformations.

Role of compression zone in shear strength enhancement

The presence of steel fibers appeared to delay the development of flexural cracks as well as reduce their rate of propagation. For this reason, the first diagonal crack in each test

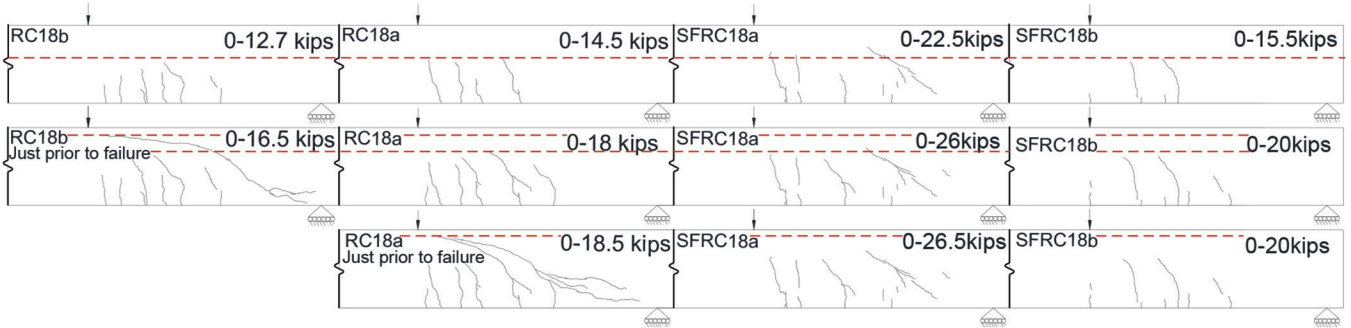


Fig. 3—Crack propagation rate comparison at same shear force increment, left to right: RC18b; RC18a; SFRC18a; and SFRC18b.

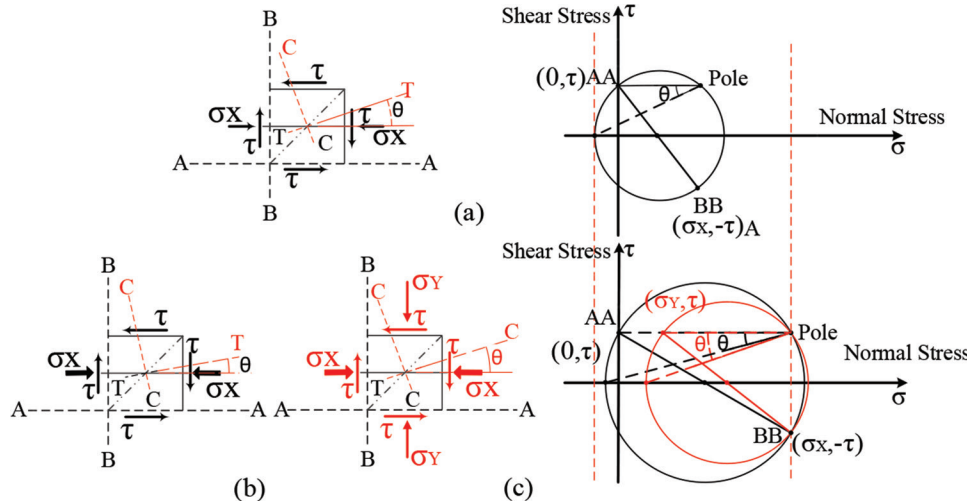


Fig. 4—Comparison of stress state and induced principal stresses in compression zone between PC and SFRC beams: (a) uniaxial stress state in PC beams; (b) uniaxial stress state in SFRC beams; and (c) biaxial stress state in SFRC beams.

SFRC beam with the exception of SFRC12W24 and SFRC18b was observed to predominantly initiate in the form of a web-shear crack with a nearly 45-degree slope rather than the flexural-shear cracks commonly seen in RC beams. Table 3 shows the first shear cracking strength (v_{cr}). Comparing v_{cr} values for SFRC 18-in.-deep specimens with RC beams of identical height indicated a 58% increase in the first shear cracking strength on average. In other words, SFRC beams were subjected to a higher load at the development of the first shear crack. This higher load also induced greater horizontal compressive stresses in the uncracked compression zone. These high horizontal compressive stresses in turn slowed down the crack propagation by reducing the principal tensile stresses. Near the loading point, the vertical compressive stresses under the load further reduced the principle tensile stress due to a biaxial compressive stress state and was able to totally stop the crack propagation. Meanwhile, the vertical compressive stresses over the support likewise limited the bond splitting along the longitudinal reinforcing bars (Ferguson et al. 1988; Untrauer and Henry 1965). Hence, an even higher load is generally required for cracks to further advance in the SFRC beams, as clearly indicated by Fig. 3. That is, the compression zone in SFRC specimens undergoes more gradual changes in the depth while the load increases. In Fig. 3, the crack propagation rates of the RC and the SFRC 18 in. deep specimens are

compared at similar shear force increments. As can be seen, a small increment (0.5 kip [2.23 kN] in shear) led to a fast propagation of the critical crack in the RC18a beam; on the other hand, there was nearly no advance of cracks in the SFRC beams at the same load increment. The slow progression of the cracks in the SFRC specimens kept the compression zone depth large, thereby enabling the compression zone to contribute to a higher shear resistance. As a result, the external load gradually increases to a value much beyond any load that an identical PC beam can carry. For this reason, the horizontal compressive stresses induced by the bending moment alone (Fig. 4(b)) or in combination with the vertical normal stresses resulting from the large applied load (Fig. 4(c)) significantly enhances the shear performance of the compression zone. Figure 4(b) shows how the existing large horizontal normal stress generated by bending moment leads the Mohr's circle to become larger in diameter and shift more to the right along the compression axes in comparison with its size and situation in plain concrete beams (Fig. 4(a)). The stress element shown in Fig. 4(a) represents the state of stress in the compression zone for a PC beam. Therefore, the consequent reduced principal tensile stresses at higher stages of loading in SFRC beams would delay the potential penetration of the existing inclined cracks into the compression zone. As demonstrated later in this paper, the penetration of a critical shear crack would lower the shear capacity of the

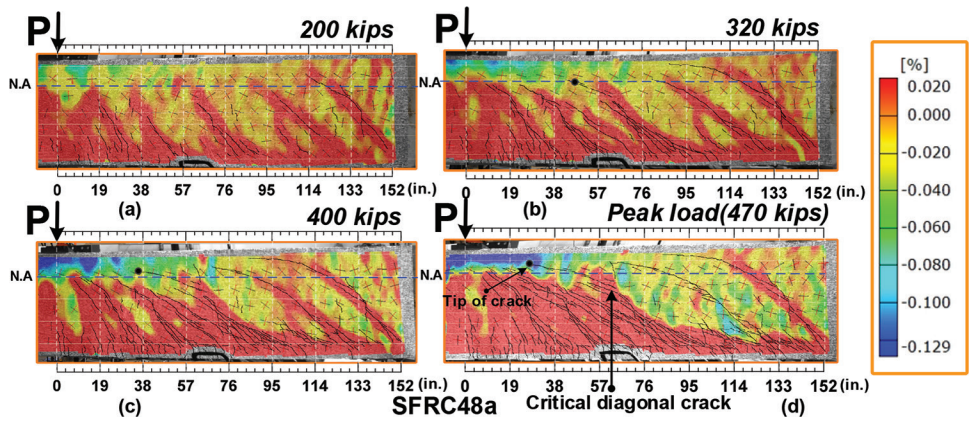


Fig. 5—Variation of depth and length of compression zone in SFRC48a during development and progression of cracks as result of load increment.

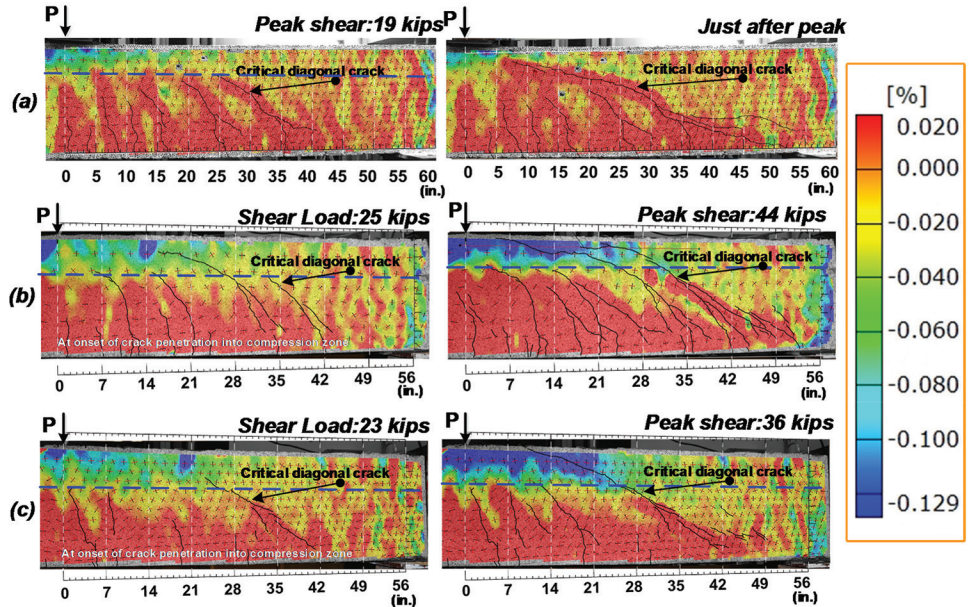


Fig. 6—Comparison of effect of critical crack propagation on depth and length of compression zone between RC and SFRC beams: (a) RC18a; (b) SFRC18b; and (c) SFRC18a.

compression zone. As moving closer to the loading point, this potentiality to cause damage could become substantially lower or even be completely eliminated due to the development of a large biaxial compressive stress state, as demonstrated in Fig. 4(c). For this reason, a large area adjacent to the loading point was observed to be free of cracks even up to failure in all the tested specimens with the exception of SFRC18b. Figure 5 displays the full field horizontal strain obtained from DIC for SFRC48a in which the tensile strains are red, while other colors (yellow to dark blue)* represent various magnitudes of compressive strain in the compression zone. For the purposes of making comparison at different loads, the total range of strain was fixed. Figure 5 indicates a slow change in both the compression zone depth and length during the loading process up to failure. Figure 5 also compares the progression status of each shear crack at different loads throughout the shear span. It can be clearly seen, as the distance from the loading point increased, the

shear cracks were more prone to penetrate into the compression zone. Nevertheless, after the penetration, the high horizontal compressive stresses in the cracked compression zone impeded the immediate advance of the penetrated cracks and the consequent abrupt failure of the beam, as noted in the PC beams. Figure 6 further illustrates the effect of the compression zone in shear strength between geometrically identical SFRC and PC beams. In Fig. 6(a), upon penetration of the shear crack into the PC beam compression zone, the crack suddenly extended all the way through the compression zone toward the loading point and resulted in beam failure. The left images of Fig. 6(b) and 6(c) show the cracking pattern for the SFRC beams at the onset of critical shear crack penetration, whereas the right images indicate the shear crack trajectories at the peak loads. As indicated by the figures, after crack penetration, SFRC specimens were able to maintain their shear resistance such that SFRC18b and SFRC18a could sustain 76% and 56% additional loads before failure, respectively.

*For visualization of color in Fig. 5, refer to online version.

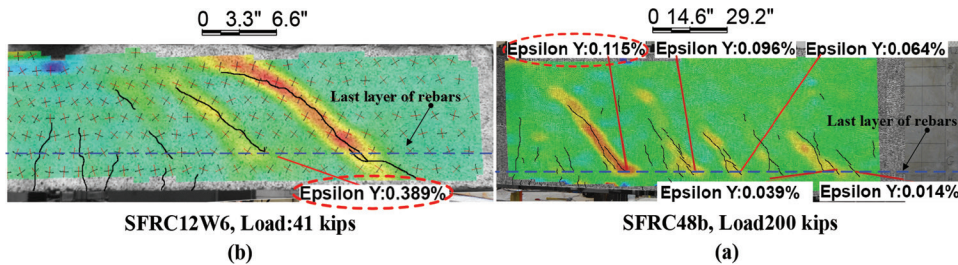


Fig. 7—Measured vertical normal strains at intersections of diagonal cracks and flexural bars: (a) SFRC48b at load of 200 kip (889 kN); and (b) SFRC12W6 at load of 41 kip (182.3 kN).

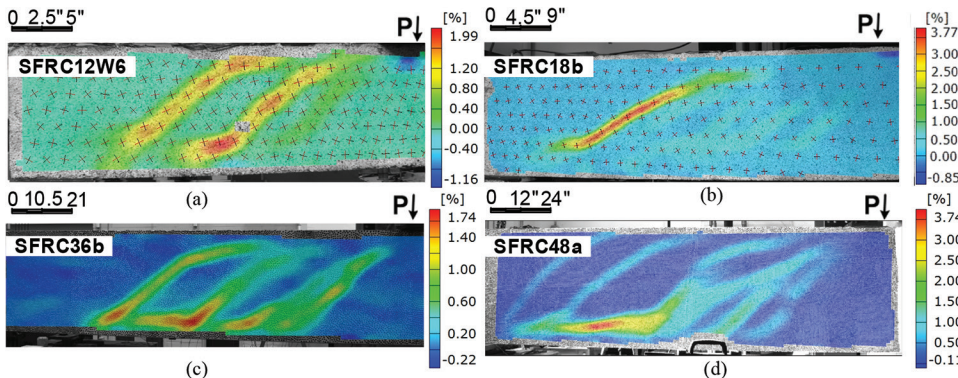


Fig. 8—Highly strained region developed in dowel zone in vertical direction (*y*-direction) at peak load: (a) SFRC12W6; (b) SFRC18b; (c) SFRC36b; and (d) SFRC48a.

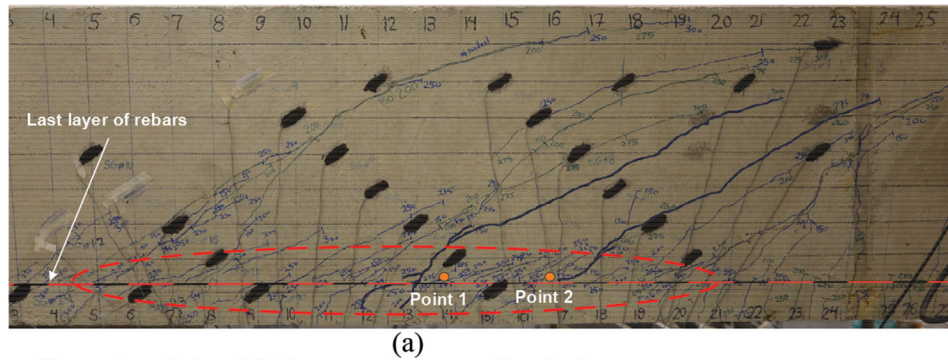
Dowel action and its effect on shear strength enhancement

The dowel strength of a PC beam is mainly a function of concrete tensile strength (Baumann 1968). Therefore, the enhanced tensile characteristic of SFRC and the effectiveness of fibers to restrict the width of dowel cracks could improve the dowel resistance. Figure 7 displays the full field vertical strains (*y*-direction) across the shear span for SFRC48b and SFRC12W6 at loads of 200 and 41 kip (890 and 182 kN), respectively. At these loads, the existing shear cracks started reaching the level of longitudinal reinforcing bars. At this time, dowel action started taking effect. This can be observed in Fig. 7, where even though no dowel cracks appeared along the longitudinal reinforcing bars, the maximum vertical strains due to dowel action were 3890 and 1150 $\mu\epsilon$ for SFRC12W6 and SFRC48b, respectively. These strains sustained by the SFRC beams were significantly greater than the dowel cracking tensile strain of PC beams (500 $\mu\epsilon$ reported by Houde and Mirza [1974]). The greater strain capability of SFRC in the dowel zone delayed the development of dowel cracks.

After initiation of the dowel crack, steel fibers can still hold the longitudinal reinforcing bars up in their original place by bridging and restricting the widening of the crack, thereby allowing them to consistently contribute to shear resistance in the form of dowel action. Therefore, the function of steel fibers could be analogous to that of stirrups in a dowel zone. On the other hand, the presence of steel fibers also slows down the propagation of dowel cracks, as observed in the test SFRC beams. Figure 8 visualizes the strains in the vertical direction (*Y*-direction) at peak load for the different beams. As will be demonstrated later, the dowel action contributes less to shear resistance for shallower SFRC beams. This observa-

tion can be recognized in Fig. 8, which gives full field strain in *y*-direction. Figures 8(c) and 8(d) show a highly strained region along the longitudinal reinforcing bars for the specimens with depths of 36 and 48 in. (914 and 1219 mm). On the other hand, as shown in Fig. 8(a) and 8(b), SFRC12W6 and SFRC18a relied less on dowel action for the shear resistance due to the greater shear resistance provided by the compression zone (discussed later).

The dowel action provided by SFRC can be seen in Fig. 9, where multiple oblique small cracks are observed rather than horizontal splitting cracks extending along the longitudinal reinforcing bars. Orientation of the cracks became flatter as they moved away from the intersections of the shear cracks and longitudinal reinforcing bars. The flatter inclination of the cracks was a result of the reduced tensile stresses developed in the surrounding SFRC along the bars due to the dowel force. This observation can be explained by using the stress state of two given points, as shown in Fig. 9(a). Unlike plain concrete, SFRC surrounding the longitudinal reinforcing bars is able to carry part of the tensile force induced by the bending moment as well as part of the shear force carried by the dowel zone. The consequent stresses are shown by σ_x and τ , respectively. Furthermore, the vertical tensile stress denoted by σ_y is the tensile stress formed along the longitudinal reinforcing bars in SFRC due to the dowel action of longitudinal reinforcing bars. The mechanical analysis given in Fig. 9(b) through 9(d) proves that these stresses, and hence the dowel action, must be present to form such cracks oriented along the longitudinal reinforcing bars. Figure 9(a) clearly shows that, despite the development of a large number of dowel cracks, the presence of steel fibers preserved the contribution of dowel action to shear resistance.



(a)

τ : Shear stress induced in the concrete surrounding the bars
 σ_y : Vertical tensile stress developed in the material due to dowel action of reinforcement bars
 σ_x : Horizontal tensile stress developed in the material arising from bending moment

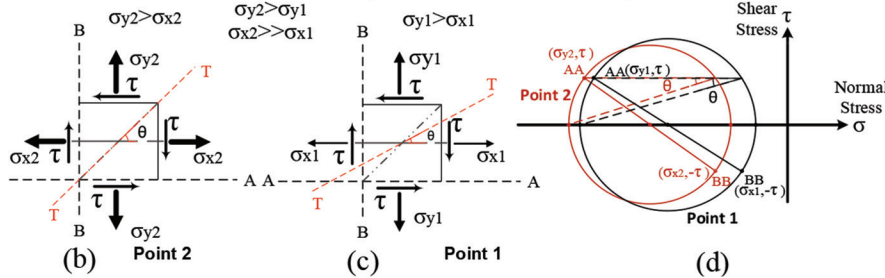


Fig. 9—(a) View of inclined dowel cracks; (b) state of stress induced in dowel zone adjacent to diagonal crack, Point 2; (c) state of stress in dowel zone away from diagonal crack, Point 1; and (d) Mohr's circles representing states of stress in Points 1 and 2.

Aggregate interlock

Aggregate interlock has been considered the primary factor contributing to the shear resistance of slender PC beams. In other words, in PC beams, when the current shear stress exceeds aggregate interlock capacity, the beam fails in shear (Fenwick and Paulay 1968; Vecchio and Collins 1986).

Laboratory test results have shown that a PC beam is approaching shear failure when the maximum width along the critical crack reaches ultimately a value of approximately 0.02 in. (0.5 mm), generally irrespective of the beam size and aggregate type and size. Sherwood (2008) observed that the maximum width along the critical crack at failure for the deeper specimens ($h = 59.4$ in. [1510 mm]) was in the range of 0.016 to 0.02 in. (0.4 to 0.5 mm), whereas the critical crack width became narrower when the height of specimens (h) decreased to 13 in. (330 mm), ranging between 0.002 to 0.004 in. (0.05 to 0.1 mm). Minelli et al. (2014) reported the maximum width of critical crack at failure between 0.01 and 0.02 in. (0.25 and 0.50 mm) for their PC beams, where the beam height varied from 20 to 59 in. (500 to 1500 mm). For the present study, the maximum crack widths at peak loads C_w for the specimens are listed in Table 3. The associated values for the pair of PC beams are 0.001 and 0.014 in. (0.04 and 0.35 mm), which are consistent with values from past research.

While aggregate interlock likely has already vanished in the vicinity of the maximum crack width, the other points along the critical crack path are still narrower, thereby maintaining shear resistance. Therefore, to determine the percentage of aggregate interlock's contribution to the total shear resistance, the maximum crack width allowing the aggregate interlock to exist needs to be determined. Push-off specimens were tested, and the crack widths right before failure along the failure plane were measured by the DIC system. Figures 10(a) and

10(b) show typical results of the crack width distribution prior to the loss of aggregate interlock, and the average width of crack was 0.008 in. (0.2 mm). This value is approximately close to the lower-bound maximum measured crack width in the aforementioned results by other researchers.

According to Walraven (1981) and Reinhardt and Walraven (1982), the net shear resistance perpendicular to a beam axis at any point along a crack resulting from aggregate interlock is an interaction between shear stress acting on cracked plane, normal stress acting on cracked plane, crack width, and crack slip (Fig. 10(c)). Based on extensive push-off tests, they proposed the following equations to express this interaction (Reinhardt and Walraven 1982)

$$\tau = -\frac{f'_c}{30} + [490 w^{-0.80} + (0.61 w^{-0.707} - 5.1)f'_c]\Delta \quad \tau \geq 0 \text{ (psi, in.)} \quad (1a)$$

$$\sigma = -\frac{f'_c}{20} + [638 w^{-0.63} + (0.81 w^{-0.552} - 3.81)f'_c]\Delta \quad \sigma \geq 0 \text{ (psi, in.)} \quad (1b)$$

where τ is shear stress acting on cracked plane at each point along the critical crack; σ is normal stress acting on cracked plane; and w and Δ are crack width and crack slip, respectively.

To evaluate the contribution of aggregate interlock to shear resistance, the distributions of crack width and crack slip along the critical crack were determined through DIC analysis for each SFRC specimen at its peak shear strength. At each point along the critical crack, the corresponding interface shear and normal stresses (Fig. 10(c)) were computed by using Eq. (1).

In this research, the shear resistance from aggregate interlock at any point with a crack width exceeding 0.008 in. (0.2 mm)

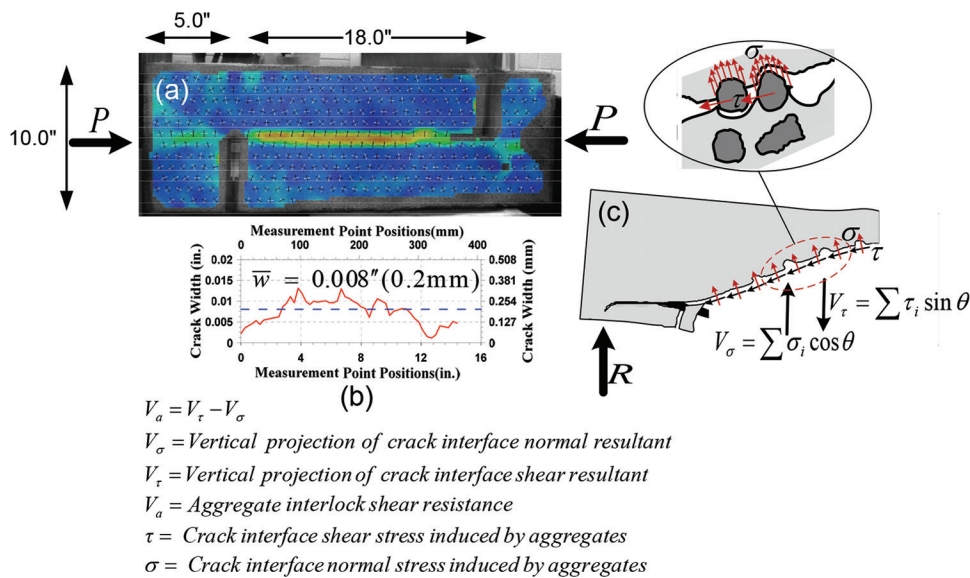


Fig. 10—(a) Push-off specimen and crack widths measured by DIC; (b) distribution of crack width along failure path right prior to failure; and (c) shear and normal stresses induced on crack faces.

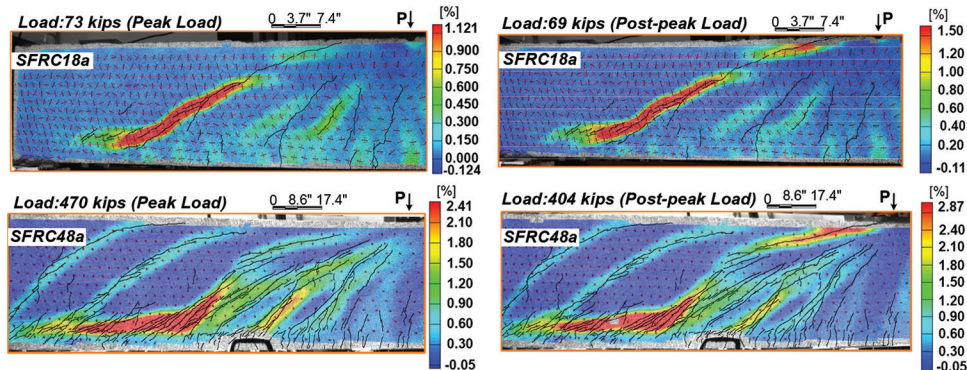


Fig. 11—Visualization of full field maximum principal strain across shear span for SFRC18a and SFRC48a (Type I failure mode).

was assumed to be zero. Lastly, as shown in Fig. 10(c), the net total vertical shear resistance induced by aggregate interlock was calculated by subtracting the vertical component of the crack interface normal resultant V_σ from the vertical component of the crack interface shear resultant V_τ . The calculation indicates that the contribution of aggregate interlock to shear resistance ranged between 0 to 1% for SFRC specimens, except for SFRC48a, for which the value is 5%. This low contribution from aggregate interlock is understandable because, everything else being the same, due to compatibility, crack width of the critical crack will be greater if a beam has a greater deflection. For example, for the 18 in. (457 mm) RC and SFRC beams (refer to Table 3), both of the deflections and maximum crack widths of the SFRC beams are much larger than that of the RC beams. The authors' assessment indicates aggregate interlock in general has a minor contribution at the point where the beams reach their peak strengths; therefore, it is conservatively neglected in this study.

it is imperative to first identify the cause leading to the drop in shear strength of SFRC beams to apply the correct failure criterion.

Two types of failure modes were observed: In Type 1 failure, a major diagonal crack occurred in the compression zone followed by an immediate drop in shear strength. Dowel action was able to carry the residual strength after the compression zone failure (Fig. 11). In Type 2 failure, the compression zone and dowel action failure occurred nearly at the same time and could not be easily distinguished by the naked eye or video. Nevertheless, the DIC images shown in Fig. 12 clearly show that, at the time the specimens reached their peak strength, the strains at the dowel zone remain the same while the principal tensile strains at the upper part of the critical diagonal cracks (circled by dashed lines) become much larger, which triggers the failure of the compression zone. Therefore, in either Type 1 or Type 2 failure, the drop in shear strength was initiated by the tension failure of the compression zone.

SHEAR RESISTANCE MECHANISM

Critical factor leading to drop of peak shear strength

The major contributors to the shear resistance of SFRC beams is provided by the compression zone, steel fiber bridging along the critical crack, and dowel action. However,

Contribution of each component to ultimate shear strength

Fiber bridging—Steel fibers crossing a diagonal crack resist shear forces by means of the vertical component of

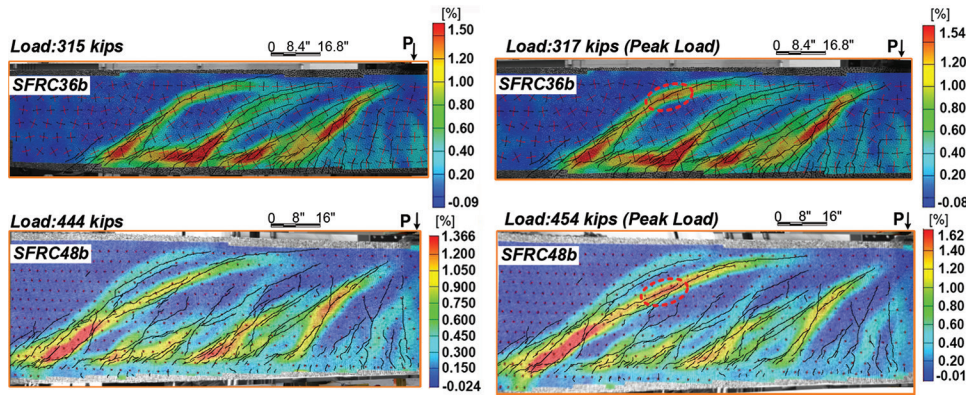


Fig. 12—Visualization of full field maximum principal strain across shear span for SFRC36b and SFRC48b (Type 2 failure mode).

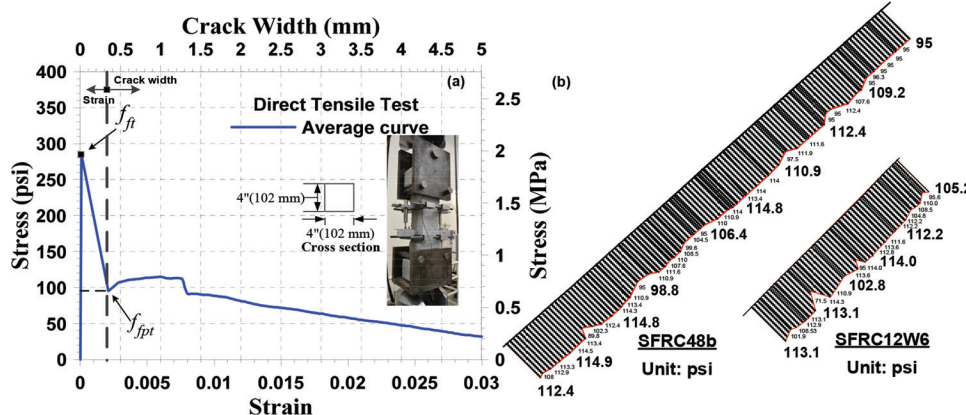


Fig. 13—(a) Average tensile stress crack with response of SFRC material used in this study; and (b) distribution of SFRC tensile stress along critical crack for two specimens: SFRC48b and SFRC12W6.

the tensile stresses developed across the crack. Magnitude of the tensile stresses of SFRC depends on the crack width, as shown in Fig. 13(a), in which the average of tensile stresses of six specimens under direct tensile test is plotted with respect to crack widths. The crack width distribution along the critical crack at the peak load for the large-scale beam specimens was measured by the DIC system. To determine the stress at each point along the critical crack, the stress for a particular point was picked from the stress-crack width curve, as given in Fig. 13(a). Next, the curved crack path was divided into a series of straight lines with corresponding angles; then, the stress distribution and corresponding resultant force were computed along each line and projected in the vertical direction based on its angle. Finally, all calculated forces were added together to represent the contribution of steel fiber bridging in resisting the total shear at peak load. Figure 13(b) displays the magnitude and distribution of the tensile stress along the critical crack for SFRC12W6 and SFRC48b. Figure 13(b) gives the stress distribution along the entire length of the critical crack in the tension zone. For clarity, the distribution was plotted on a straight line rather than along the curved crack. The shear force carried by steel fibers crossing the critical crack in the tension zone (that is, below the neutral axis) and the percentage of its contribution to the total shear at peak load for all the specimens are listed in Columns 2 and 5 of Table 4, respectively.

Proportion of shear force carried by compression zone at peak load

Shear strength of the compression zone in an SFRC beam can be controlled by either compression or tension mode of failure (Choi et al. 2007; Kotsovos and Pavlović 1998). Because concrete's compressive strength is much larger than its tensile strength, the shear failure of the compression zone is typically initiated by tensile cracking (Choi et al. 2007; Kotsovos and Pavlović 1998). The tension-induced failure typically results in propagation of the critical crack all the way through the compression zone depth. Based on a mechanical based analysis, Choi et al. (2007) demonstrated that the shear failure of the compression zone of an SFRC beam is dominated by tension. Their conclusion was also confirmed by the test observation in the present study, as shown in Fig. 11 and 12. For this reason, to estimate the shear capacity of the compression zone for the SFRC specimens, Rankin's failure criteria was adopted with the same approach as employed by Choi et al. (2007), which takes into account the interaction between the shear and compressive stresses. As observed in this study's tests (Fig. 5), before failure, the critical crack had already extended into the compression zone and, hence, the shear failure of the compression zone was assumed to occur when the principal tensile stress at each point along the penetrated critical crack reaches the post-cracking tensile strength of SFRC (Eq. (2a) and (2b)). At the same time, the principal tensile stress along the intact failure path attains the peak tensile strength of the

Table 4—Contribution of main shear components and their percentage in shear capacity

Specimen	V_{sf} , [*] kip (kN)	V_{uc} , [†] kip (kN)	V_u , [‡] kip (kN)	V_{sf}/V_u , %	V_{uc}/V_u , %	V_d/V_u , %
SFRC12W6	5.5 (24)	18.7 (83)	27.0 (120)	20.4	69.2	10.4
SFRC12W24	36.9 (164)	60.2 (268)	108.0 (480)	34.2	55.8	10.0
SFRC18a	8.7 (39)	23.1 (103)	36.0 (160)	24.2	64.3	11.5
SFRC18b	10.5 (47)	23.1 (103)	44.0 (196)	23.9	52.6	23.5
SFRC36b	35.5 (158)	71.1 (316)	158.0 (703)	22.5	45.0	32.5
SFRC48a	34.6 (154)	118.6 (528)	235.0 (1045)	14.7	50.5	34.8
SFRC48b	67.7 (301)	81.8 (364)	227.0 (1010)	29.8	36.0	34.2

*Shear resisted by steel fiber in tension zone at peak.

[†]Shear resisted by compression zone at peak.

[‡]Measured ultimate shear resistance.

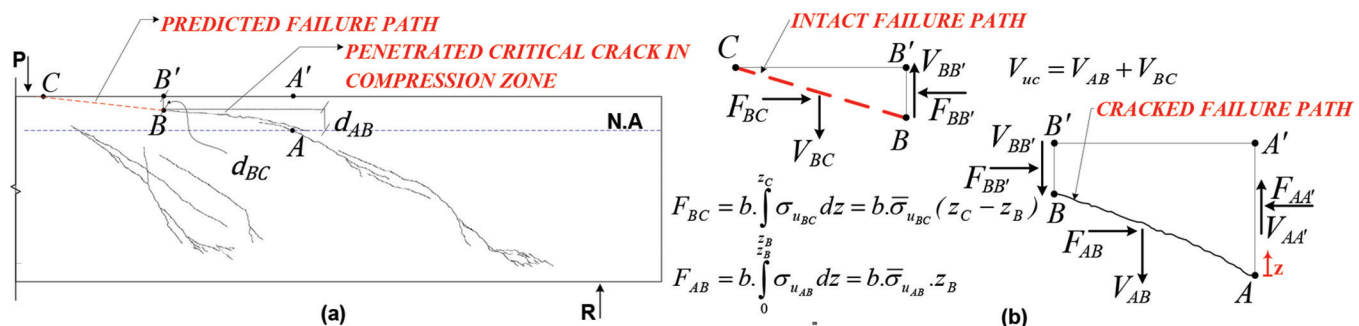


Fig. 14—Schematic view of: (a) cracked and intact failure path in compression zone; and (b) resultant forces acting along cracked and intact failure path.

SFRC material. The peak and post-cracking tensile strengths of the SFRC were acquired from direct tensile tests at 285 and 95 psi (1.96 and 0.65 MPa) (Fig. 13(a)), respectively. These results are close to the corresponding values of 242 and 91 psi (1.67 and 0.62 psi) computed from the equations proposed by Naaman (2002) and Naaman and Reinhardt (2003) for the properties of steel fibers (steel fiber type, volume fraction, and fiber aspect ratio) and concrete (tensile strength) used in this study. Rankin's failure criterion predicting tensile failure in the compression zone along the cracked and uncracked failure paths is mathematically expressed as shown in Fig. 14(a) and in Eq. (2a) and (2b)

$$-\frac{\sigma_{u_{AB}}}{2} + \sqrt{\left(\frac{\sigma_{u_{AB}}}{2}\right)^2 + v_{u_{AB}}^2} = f_{fpt}$$

(along penetrated critical crack in compression zone) (2a)

$$-\frac{\sigma_{u_{BC}}}{2} + \sqrt{\left(\frac{\sigma_{u_{BC}}}{2}\right)^2 + v_{u_{BC}}^2} = f_{ft} \quad (\text{along failure path}) \quad (2b)$$

where f_{ft} and f_{fpt} are peak and post-cracking tensile strengths of SFRC obtained from direct tensile tests (Fig. 13a), respectively; $\sigma_{u_{AB}}$ and $v_{u_{AB}}$ are the normal compressive and shear stresses at each given point along the critical crack in the compression zone (Fig. 14(a), Path AB); and $\sigma_{u_{BC}}$ and $v_{u_{BC}}$

are the normal compressive and shear stresses, respectively at any point along the uncracked failure path in the compression zone (as shown in Fig. 14(a), Path BC).

Rearranging the shear stress in Eq. (2a) and (2b) gives the allowable shear stresses along the failure paths (a function of compressive stress at each given point), which is expressed as

$$v_{u_{AB}} = \sqrt{f_{fpt}(f_{fpt} + \sigma_{u_{AB}})}$$

(along penetrated critical crack in compression zone) (3a)

$$v_{u_{BC}} = \sqrt{f_{ft}(f_{ft} + \sigma_{u_{BC}})} \quad (\text{along failure path}) \quad (3b)$$

By integrating Eq. (3a) and (3b) over an infinitesimal vertical surface ($dA = b \times dz$, where b is the width of cross section and z is the vertical distance measured from neutral axis) along paths AB and BC, one can find the resultant vertical force acting along the failure path in the compression zone (AB and BC in Fig. 14(b)). The numerical expression is found as Eq. (4a) and (4b)

$$V_{AB} = b \int_0^{z_B} \sqrt{f_{fpt}(f_{fpt} + \sigma_{u_{AB}})} dz$$

(along penetrated critical crack in compression zone) (4a)

$$V_{BC} = b \int_{z_B}^{z_C} \sqrt{f_{ft}(f_{ft} + \sigma_{u_{BC}})} dz \quad (\text{along the failure path}) \quad (4b)$$

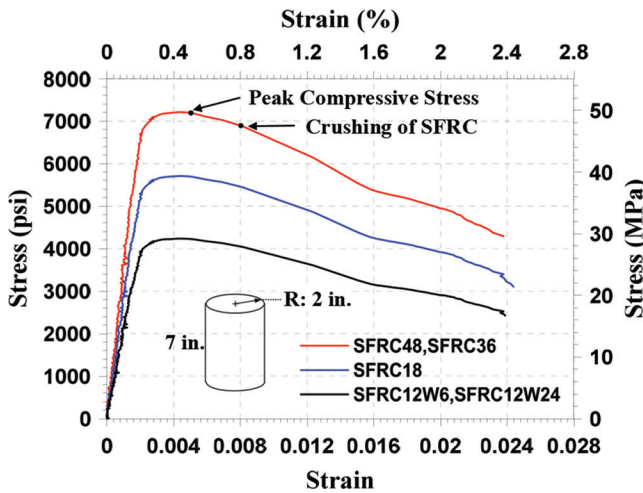


Fig. 15—Average stress-strain relationships for sampled SFRC cylinders.

To simplify the computations, the current compressive stress functions in Eq. (4a) and (4b) along the cracked and intact failure paths were replaced with the average compressive stress (discussed later) denoted by $\bar{\sigma}_{u_{AB}}$ and $\bar{\sigma}_{u_{BC}}$ in Eq. (5a) and (5b), respectively

$$V_{AB} = b \cdot \int_{z_A}^{z_B} \sqrt{f_{fpt}(f_{fpt} + \bar{\sigma}_{u_{AB}})} dz = \sqrt{f_{fpt}(f_{fpt} + \bar{\sigma}_{u_{AB}})} b \cdot d_{AB} \quad (5a)$$

$$V_{BC} = b \cdot \int_{z_B}^{z_C} \sqrt{f_{ft}(f_{ft} + \bar{\sigma}_{u_{BC}})} dz = \sqrt{f_{ft}(f_{ft} + \bar{\sigma}_{u_{BC}})} b \cdot d_{BC} \quad (5b)$$

where d_{AB} and d_{BC} are the vertical distance between points A and B , respectively, as can be seen in Fig. 14(a); the vertical distance between points B and C are in Fig. 14(a).

The maximum shear force V_{uc} resisted by the compression zone is considered the sum of V_{AB} and V_{BC} , which are expressed as

$$V_{uc} = V_{AB} + V_{BC} \quad (6)$$

In Eq. (5a) and (5b), to determine the average of compressive stresses, $\bar{\sigma}_{u_{AB}}$ and $\bar{\sigma}_{u_{BC}}$, generated by the bending moment, the distribution of the compressive strains along paths AB and BC were first obtained by using the DIC system for each test beam at the peak load. Then, the corresponding compressive stress of each strain along paths AB and BC was found from the stress-strain relationship obtained from the SFRC cylinder tests (Fig. 15). To be consistent, the strains of the cylinders were also measured by the DIC system. Lastly, the average compressive stresses, $\bar{\sigma}_{u_{AB}}$ and $\bar{\sigma}_{u_{BC}}$, were calculated based on the compressive stress distributions along paths AB and BC . The maximum shear force carried by the compression zone at peak load and the percentage of its contribution to the total shear resistance are presented in Columns 3 and 6 of Table 4, respectively. The remaining percentage of shear resistance was attributed to the contribution of dowel action as

noted in the last column of Table 4. As can be seen, the shear resistance proportion of the compression zone decreases from 69 to 36% when the beam depth increased from 12 to 48 in. (305 to 1220 mm). However, for the same range of changes in the beam depth, the dowel action contribution was found to vary from 10% to 35%, depending on the increase in beam depth. On the other hand, the percentage of steel fiber contribution is constant for all the SFRC beams regardless of their depths. These analyses give consistent results as observed from the DIC images as shown in Fig. 8.

Effect of width on shear strength of SFRC beams (in terms of stress)

As discussed in the previous section, the width of each specimen in this study was adjusted in recognition of the negligible effect of width on the ultimate shear strength of RC beams (Kani et al. 1979; Lubell et al. 2004). This study investigated the validity of this observation on SFRC beams. For this purpose, two SFRC specimens (SFRC12W6 and SFRC12W24) with a total height of 12 in. (305 mm) were constructed. Their widths were 6 and 24 in. (152 and 610 mm), respectively. Test results from this study (Table 3) indicate that, similar to the observation for PC beams, the width of SFRC beams has no effect on ultimate shear strength. The ultimate shear stresses at failure for SFRC12W6 and SFRC12W24 were identical at $6.9\sqrt{f'_c}$ psi.

Arch action involvement in strength-enhancement mechanism

Arch action is an alternative shear-strength-enhancement mechanism that might develop in a PC beam after beam action is destroyed due to the complete loss of bond between the longitudinal reinforcing bars and concrete (Park and Paulay 1975). In other words, the longitudinal reinforcing bars sustain nearly the same strain throughout the length. Prior research carried out by Sneed and Ramirez (2010) on the shear strength of geometrically equivalent PC beams with different heights indicated a higher chance of arch action development for the beams with the smallest height (12 in. [305 mm]). Therefore, in this study, the smallest SFRC specimens were selected for arch action investigation. A series of strain gauges were mounted on one of the bottom-layer reinforcing bars in the shallowest specimens (SFRC12W6 and SFRC12W24). The first 12 gauges were spaced 3 in. (76 mm) apart, starting from midspan up to the center of support, while the remaining two were spaced evenly at 1.5 in. (38 mm) passing the center of support toward the anchorage (Fig. 16). Figure 16 shows the variation of measured strains along the reinforcing bars in SFRC12W6 and SFRC12W24 at the peak loads. Apart from the length being in the vicinity of the midspan and accounting for one-third of the shear span length, non-uniform distribution of strains observed along the longitudinal reinforcing bars indicated a lack of either debonding or yielding of the reinforcing bars, which is necessary for the development of arch action. Therefore, no evidence was produced to indicate that any arch action contributed to the shear-enhancement mechanism.

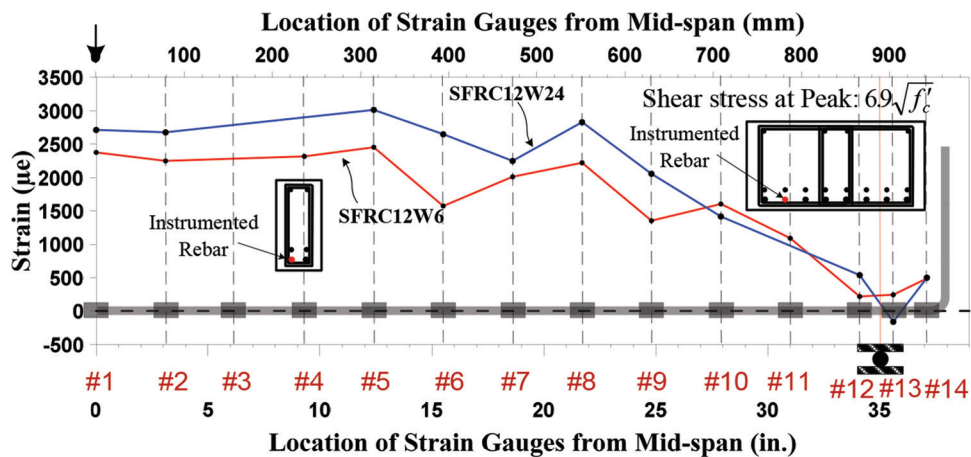


Fig. 16—Variation of longitudinal strain along reinforcing bar in SFRC12W6 and SFRC12W24 at peak shear stress (Note: f'_c in psi; 1 psi = 0.0069 MPa.)

SUMMARY, CONCLUSIONS, AND DESIGN RECOMMENDATIONS

This research examines the shear strength-enhancement and failure mechanisms of SFRC slender beams by using the full field strains obtained from digital image correlation (DIC) technology. A total of 12 large-scale simply supported SFRC and RC beams with an overall height from 12 to 48 in. (305 to 1220 mm) were tested under monotonic point load up to failure. Testing was carried out 502 to 1005 days after casting. The specimens were exposed to weather during this period. Based on the findings, the following conclusions were drawn:

1. Contrary to the conventional assumption—that is, the greater shear strength of SFRC beams directly comes from fiber bridging stress across the shear cracks—the research in this study confirmed that the first and primary factor toward shear strength enhancement of SFRC slender beams lies in the delay that takes place on the development and propagation of diagonal shear cracks, which in turn leads the compression zone to retain a larger depth, even at higher loads. The deeper and highly compressed compression zone will then contribute to a higher shear resistance. DIC analysis showed that the compression zone of an SFRC beam could remain stable even when shear cracks are propagated into it.

2. From the full field deformations measured by the DIC technique and the mechanical-based computation, dowel action is recognized as one of the major contributions to shear resistance of SFRC beams.

3. The results from this study indicate that ultimate shear strength of an SFRC beam is provided through three primary components, including shear force developed in the compression zone, shear force arising from dowel action of the longitudinal reinforcing bars, and the vertical component of tension induced in the steel fibers crossing the critical diagonal crack. For SFRC beams with 0.75% fiber volume fraction, dowel action accounts for 10 to 35% of the total shear capacity when the height varies from 12 to 48 in. (305 and 1220 mm). Meanwhile, for this range of beam height, the compression zone contribution decreases from 69 to 36% of the total shear resistance. However, the steel fiber

bridging effect was observed to remain constant at approximately 20%.

4. The contribution of aggregate interlock to the ultimate shear strength was determined negligible based on experimental testing and a computation using the interaction of shear stress acting on the cracked plane, normal stress acting on cracked plane, crack width, and crack slip.

5. According to the measured strain profiles of longitudinal reinforcing bars, no evidence indicates that arch action contributes to the shear-enhancement mechanism.

6. The ultimate shear strengths obtained from the series of tests on SFRC beams were all in excess of $5\sqrt{f'_c}$. Therefore, the maximum factored shear stress of $2\phi\sqrt{f'_c}$ (that is, $1.5\sqrt{f'_c}$, where $\sqrt{f'_c}$ is in psi) allowed by ACI Committee 318 (2014) is very conservative. Therefore, it is suggested that this maximum factored shear stress can be safely raised to $4\phi\sqrt{f'_c}$ (that is, $3\sqrt{f'_c}$, where f'_c is in psi). It is recognized that the dispersion and alignment of the fibers are in a random manner and a statistical treatment of data is warranted to further refine the maximum factored shear stress allowed in ACI 318.

AUTHOR BIOS

ACI member Mohammad Reza Zarrinpour is a Structural Engineer at Huitt-Zollars, Dallas, TX. He received his PhD from the Department of Civil Engineering at the University of Texas at Arlington, Arlington, TX. His research interests include analysis and design of fiber-reinforced concrete structures.

ACI member Shih-Ho Chao is an Associate Professor at the University of Texas at Arlington. He is a member of the ACI Committees 239, Ultra-High Performance Concrete, and 544, Fiber-Reinforced Concrete. He received the ACI Chester Paul Siess Award for Excellence in Structural Research in 2011. His research interests include fiber-reinforced concrete and seismic behavior of reinforced concrete structures.

ACKNOWLEDGMENTS

The SFRC specimens were cast at Forterra Pipe & Precast in Grand Prairie, TX, V. Babakhanian, and their workers. Steel fibers were provided by Maccaferri. G. Parra-Montesinos at the University of Wisconsin-Madison reviewed the design of the specimens. J.-S. Cho greatly contributed to specimen design and construction. Each person and company represented herein offered essential help that is gratefully appreciated. Also, special thanks goes to P. Hajalikhani, C. Jiansinlapadamrong, and R. Waweru, the members of our research group at the University of Texas at Arlington, each of whom greatly assisted in this research.

REFERENCES

- ACI Committee 318, 2014, "Building Code Requirements for Structural Concrete (ACI 318-14) and Commentary (ACI 318R-14)," American Concrete Institute, Farmington Hills, MI, 519 pp.
- Baumann, H., 1968, "Tests to Study the Dowel Action of the Bending Tension Reinforcement of Reinforced Concrete Beams," *Bericht Nr. 77*, Munich Technischen Hochschule.
- Bresler, B., and Pister, K. S., 1958, "Strength of Concrete under Combined Stresses," *ACI Journal Proceedings*, V. 55, No. 9, Sept., pp. 321-345.
- Choi, K. K.; Park, H. G.; and Wight, J. K., 2007, "Shear Strength of Steel Fiber-Reinforced Concrete Beams without Web Reinforcement," *ACI Structural Journal*, V. 104, No. 1, Jan.-Feb., pp. 12-21.
- Dinh, H. H.; Parra-Montesinos, G. J.; and Wight, J. K., 2010, "Shear Behavior of Steel Fiber Reinforced Concrete Beams without Stirrup Reinforcement," *ACI Structural Journal*, V. 107, No. 5, Sept.-Oct., pp. 597-606.
- Dinh, H. H.; Parra-Montesinos, G. J.; and Wight, J. K., 2011, "Shear Strength Model for Steel Fiber Reinforced Concrete Beams without Stirrup Reinforcement," *Journal of Structural Engineering*, ASCE, V. 137, No. 10, pp. 1039-1051. doi: 10.1061/(ASCE)ST.1943-541X.0000362
- Fenwick, R. C., and Paulay, T., 1968, "Mechanisms of Shear Resistance of Concrete Beams," *Journal of the Structural Division*, ASCE, V. 94, No. 10, pp. 2325-2350.
- Ferguson, P. M.; Breen, J. E.; and Jirsa, J. O., 1988, *Reinforced Concrete Fundamentals*, fifth edition, John Wiley & Sons, Inc., New York, 768 pp.
- Houde, J., and Mirza, M. S., 1974, "A Finite Element Analysis of Shear Strength of Reinforced Concrete Beams," *Shear in Reinforced Concrete*, SP-42, American Concrete Institute, Farmington Hills, MI, pp. 103-128.
- Joint ASCE-ACI Committee 426, 1973, "The Shear Strength of Reinforced Concrete Members," *Journal of the Structural Division*, V. 99, No. 6, pp. 1091-1187.
- Kani, M. W.; Huggins, M. W.; and Wittkopp, R. R., 1979, *Kani on Shear in Reinforced Concrete*, University of Toronto Press, Toronto, ON, Canada, 225 pp.
- Kotsovos, M. D., 1988, "Compressive Force Path Concept: Basis for Reinforced Concrete Ultimate Limit State Design," *ACI Structural Journal*, V. 85, No. 1, Jan.-Feb., pp. 68-85.
- Kotsovos, M. D., and Pavlović, M. N., 1998, *Ultimate Limit-State Design of Concrete Structures: A New Approach*, Thomas Telford, London, UK, 208 pp.
- Lubell, A.; Sherwood, T.; Bentz, E. C.; and Collins, M. P., 2004, "Safe Shear Design of Large, Wide Beams," *Concrete International*, V. 26, No. 1, Jan., pp. 66-78.
- Minelli, F.; Conforti, A.; Cuena, E.; and Plizzari, G., 2014, "Are Steel Fibres Able to Mitigate or Eliminate Size Effect in Shear?" *Materials and Structures*, V. 47, No. 3, pp. 459-473. doi: 10.1617/s11527-013-0072-y
- Mobasher, B., 2012, *Mechanics of Fiber and Textile Reinforced Cement Composites*, CRC Press, Boca Raton, FL, 473 pp.
- Muttoni, A., and Fernández Ruiz, M., 2008, "Shear Strength of Members without Transverse Reinforcement as a Function of the Critical Shear Crack Width," *ACI Structural Journal*, V. 105, No. 2, Mar.-Apr., pp. 163-172.
- Naaman, A. E., 2002, "Toughness, Ductility, Surface Energy and Deflection-Hardening FRC Composites," *Proceedings of the JCI International Workshop on Ductile Fiber Reinforced Cementitious Composites (DRFCC)—Application and Evaluation* (DFRCC-2002), Japan Concrete Institute, Tokyo, Japan, pp. 33-57.
- Naaman, A. E., and Reinhardt, H. W., 2003, "High Performance Fiber-Reinforced Cement Composites: HPFRCC 4," *RILEM Proceedings Pro 30*, RILEM Publications S.A.R.L., pp. 95-113.
- Park, P., and Paulay, T., 1975, *Reinforced Concrete Structures*, John Wiley & Sons, Inc., New York, 769 pp.
- Parra-Montesinos, G. J., 2006, "Shear Strength of Beams with Deformed Steel Fibers," *Concrete International*, V. 28, No. 11, Nov., pp. 57-66.
- Reinhardt, H. W., and Walraven, J. C., 1982, "Cracks in Concrete Subject to Shear," *Journal of the Structural Division*, V. 108, pp. 207-224.
- Sherwood, E. G., 2008, "One-Way Shear Behavior of Large, Lightly-Reinforced Concrete Beams and Slabs," PhD dissertation, Department of Civil Engineering, University of Toronto, Toronto, ON, Canada, 547 pp.
- Shoib, A.; Lubell, A. S.; and Bindiganavile, V. S., 2014, "Size Effect in Shear for Steel Fiber-Reinforced Concrete Members without Stirrups," *ACI Structural Journal*, V. 111, No. 5, Sept.-Oct., pp. 1081-1090. doi: 10.14359/51686813
- Sneed, L. H., and Ramirez, J. A., 2010, "Influence of Effective Depth on Shear Strength of Concrete Beams: Experimental Study," *ACI Structural Journal*, V. 107, No. 5, Sept.-Oct., pp. 554-562.
- Untrauer, R. E., and Henry, R. L., 1965, "Influence of Normal Pressure on Bond Strength," *ACI Journal Proceedings*, V. 62, No. 5, May, pp. 577-586.
- Vecchio, F. J., and Collins, M. P., 1986, "The Modified Compression Field Theory for Reinforced Concrete Elements Subjected to Shear," *ACI Journal Proceedings*, V. 83, No. 2, Mar.-Apr., pp. 219-231.
- Walraven, J. C., 1981, "Fundamental Analysis of Aggregate Interlock," *Journal of the Structural Division*, ASCE, V. 108, pp. 2245-2270.
- Wight, J. K., and MacGregor, J. G., 2012, *Reinforced Concrete: Mechanics and Design*, sixth edition, Prentice Hall, Upper Saddle River, NJ, 1168 pp.